Idealized Solutions for the Energy Balance of the Finescale Internal Wave Field*

KURT POLZIN

Department of Physical Oceanography, Woods Hole Oceanographic Institution, Woods Hole, Massachusetts

(Manuscript received 1 February 2002, in final form 24 July 2003)

ABSTRACT

Recent fine- and microstructure observations indicate enhanced finescale shear and strain in conjunction with bottom-intensified turbulent dissipation above rough bathymetry in the Brazil Basin. Such observations implicate the bottom boundary as an energy source for the finescale internal wave field. Simple analytical and numerical solutions to an equation governing the spatial and temporal evolution of the finescale wave field are described here. The governing equation implicitly treats the effects of wave breaking on the vertical propagation of internal waves through a flux representation of nonlinear transports associated with internal wave–wave interactions. These solutions identify the rate of dissipation of turbulent kinetic energy with downscale energy transports at high vertical wavenumber, resulting in an estimate of dissipation versus depth. The sensitivity of the turbulent dissipation depth profile to various environmental parameters is examined. Observed dissipation profiles and shear spectra are compared with these solutions, and an effort is made to relate the solutions and observations to extant models of internal wave generation and scattering.

1. Introduction

The rate of diapycnal mixing relates through the buoyancy equation (McDougall 1991) and vorticity dynamics (Stommel and Arons 1960) to the intensity of upwelling and horizontal circulation in the abyssal ocean. The strength of the thermohaline circulation (the processes by which dense water is formed in polar regions, sinks to great depths, and then upwells across isopycnals) is directly related to the rate of diapycnal mixing (e.g., Huang and Chou 1994). In turn, the intensity of diapycnal mixing relates to the ability of the abyssal ocean to store heat and greenhouse gases and to the influence of climate change on centennial-to-millennial time scales.

The intensity, spatial distribution, and causes of diapycnal mixing in the deep ocean have been the subject of much speculation. Advective heat budgets in semienclosed basins (e.g., Hogg et al. 1982) typically return estimates of $K \cong (1\text{–}10) \times 10^{-4}$ m^2 s^{-1}, similar to estimates of $K \cong 1 \times 10^{-4}$ m^2 s^{-1} obtained from vertical advection/diffusion models (Wyrtki 1961; Munk 1966). These abyssal estimates, however, do not appear to be appropriate for the stratified upper ocean, for which a purposeful tracer release experiment (Ledwell et al. 1993) and microstructure measurements (Gregg 1987) suggest $K \cong 0.1 \times 10^{-4}$ m^2 s^{-1}. Validation studies (Polzin et al. 1995; Gregg 1989) of internal wave–wave interaction models indicate that the background internal wave state described by the empirical Garrett and Munk [GM: Garrett and Munk (1975) as modified by Cairns and Williams (1976)] spectrum supports only weak ($K \leq 0.1 \times 10^{-4}$ m^2 s^{-1}) mixing that is independent of the background stratification rate N^2. This implies that, in order for internal wave–driven mixing to close advective heat budgets in abyssal basins, the internal wave spectrum needs to depart substantially from the GM specification.

Spatial variability is apparent in the abyssal ocean. Full-depth fine- and microstructure measurements from the Brazil Basin (Polzin et al. 1997) indicate weak ($K \leq 0.1 \times 10^{-4}$ m^2 s^{-1}) mixing that is approximately independent of depth above the smoothly sloping abyssal plains and continental rise of the western part of the basin. In contrast, above rough topography associated with the Mid-Atlantic Ridge, levels of turbulent mixing are orders of magnitude larger and increase with depth. The turbulence was sufficiently strong there to lead Polzin et al. (1997) to postulate that mixing in the eastern part of the basin was large enough to close Hogg et al.'s (1982) Brazil Basin abyssal heat budget. Data obtained during two additional cruises to the Brazil Basin further support this inference (Ledwell et al. 2000). Moreover, the abyssal flow in the southeast corner of the Brazil Basin appears to be forced by vortex stretching asso-

* Woods Hole Oceanographic Institution Contribution Number 9706.

Corresponding author address: Dr. Kurt Polzin, Department of Physical Oceanography, Woods Hole Oceanographic Institution, MS #21, Woods Hole, MA 02543.
E-mail: kpolzin@whoi.edu

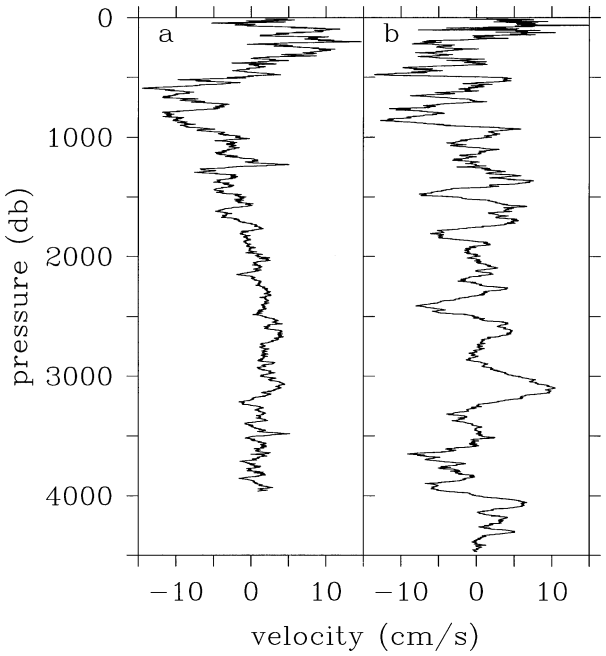

FIG. 1. Characteristic vertical profiles of horizontal (eastward) velocity obtained from the Brazil Basin. Greater velocity variance and smaller vertical coherence scales are apparent above rough topography (b) associated with the Mid-Atlantic Ridge (21.88°S, 16.36°W) than above smooth bathymetry on the western side of the basin (a) (25.00°S, 38.18°W).

ciated with this turbulent mixing (St. Laurent et al. 2001).

The above-cited investigators note enhanced velocity and density finestructure in conjunction with the increased levels of turbulent dissipation in stratified water above bottom (Fig. 1). As internal waves typically dominate the finescale flow field (e.g., Polzin et al. 2003), the association of enhanced fine- and microstructure implicates internal wave breaking as the source of turbulent energy. In particular, Polzin et al. (1997) proposed that the elevated finestructure levels were associated with a bottom-generated internal tide having horizontal scales that were characteristic of the bottom topographic roughness ($\lesssim$1000 m).

The scattering of waves incident upon bottom roughness (including an internal tide returning from the surface) transfers energy in wavenumber space and may also play a role in the local enhancement of velocity finestructure near sloping bathymetry (e.g., Müller and Xu 1992). However, such transfers are ultimately limited by the amplitude of energy sources for the incident internal wave field. In a one-dimensional (vertical) energy balance, the energy fed locally into the internal wave field by boundary sources is approximately equal to the local, depth-integrated dissipation rate. The spectral transfer by wave scattering results in a redistribution of dissipation versus depth without altering the depth-integrated dissipation rate. With values of 3–4 m W m^{-2}, depth-integrated dissipation rates are a factor of 5 larger over the Mid-Atlantic Ridge than in the western part of the Brazil Basin. This implicates additional energy sources as being responsible for the enhanced dissipation over the rough bathymetry. Circumstantial evidence for a 1D balance is provided by the observation that the depth-integrated dissipation above rough bathymetry exhibits a fortnightly modulation that is phase locked to the spring–neap transition in the barotropic tide (Ledwell et al. 2000). The predisposition in this study is to interpret the observations of enhanced fine- and microstructure above the Mid-Atlantic Ridge in terms of a local wave generation process over rough bathymetry.

This work examines the energy balance of the finescale internal wave field in the abyssal ocean. A nonlinear closure presented in a companion article (Polzin 2004) is used to examine the evolution of the internal wave spectrum with distance from the bottom boundary and predict the decay of wave energy into turbulent dissipation.

After defining equations and boundary conditions governing the spatial and temporal evolution of the finescale internal wave field (section 2), the thrust of the paper is to examine the parameter dependence of approximate solutions to this equation for a highly-idealized situation (section 3). The intent in doing so is to understand the processes that affect the magnitude and structure of the turbulent dissipation depth profile. These solutions are considered in the context of the Brazil Basin observations (section 4). The relationship of the idealized solutions and observations to extant models of internal wave generation and scattering is then discussed in section 5. The findings are summarized in section 6. Ancillary analysis of wave generation models and a scale analysis motivating the use of a one-dimensional version of the radiation balance equation are presented in an appendix.

2. A radiation balance equation

a. Description

1) THE RADIATION BALANCE EQUATION

The spatial and temporal evolution of the internal wave field can be expressed as an energy conservation statement (Polzin 2004) in the spectral domain:[1]

$$\frac{\partial E^{\pm}}{\partial t} \pm \frac{\partial (C_{gz} E^{\pm})}{\partial z} + \frac{\partial F^{\pm}}{\partial m} + \frac{\partial G^{\pm}}{\partial \omega} = \frac{1}{2m}(F^{\mp} - F^{\pm}) + \frac{1}{2}\frac{(G^{\mp} - G^{\pm})}{\varphi}\frac{\partial \varphi}{\partial \omega}. \quad (1)$$

[1] $E^{\pm} \equiv E^{\pm}(m, \omega, z, t)$ is the vertical wavenumber–frequency energy density with direction of energy propagation denoted by either + or −. In the following, the depth (z) and time (t) dependence is regarded as implicit. Here $E^{\pm}$ is the sum of kinetic ($E_k^{\pm}$) and potential ($E_p^{\pm}$) energy, $E^{\pm} = E_k^{\pm} = E_p^{\pm}$. The notation $E^{\pm}(m)$ [or $F^{\pm}(m)$] denotes integration over the frequency domain, $E^{\pm}(m) = \int E^{\pm}(m, \omega)\, d\omega$. Similarly, $E \equiv E^{+} + E^{-}$.

Here the vertical group velocity $C_{gz} = |(\omega^2 - f^2)(N^2 - \omega^2)/\omega m(N^2 - f^2)|$, and the propagation direction is given explicitly. This equation defines the evolution of the energy density in vertical wavenumber–frequency space as a function of vertical coordinate and time. The wave field has been assumed to be horizontally homogeneous; thus (1) represents a vertical balance for the energy spectrum. A scale analysis of the associated 2D radiation balance equation (appendix) justifies this approximation. The first term in (1) is the time rate of change of energy density, the second is the spatial flux divergence. The functions F and G are flux representations of spectral transports in the vertical wavenumber and frequency domains associated with wave–wave interactions. In this representation of the energy equation, there are no explicit sources of energy associated with wave generation or sinks associated with turbulent dissipation. Internal wave generation is prescribed as a boundary condition on the energy flux, and wave dissipation is equated with the transport $F(m)$ at high wavenumber.

Wave–wave interactions encompassed by the closures F and G rearrange energy in the spectral domain. The right-hand-side of (1) ensures that these rearrangements also conserve linear wave momentum [$\mathbf{P} = \mathbf{k}E/\omega$, in which $\mathbf{k}$ is the 3D wave vector (k, l, m)] and can be interpreted as a backscattering of wave energy at a rate proportional to the transports $F^{\pm}$ and $G^{\pm}$.

A prescription for the transport $F^{\pm}$ is (Polzin 2004)

$$F^{\pm}(m, \omega) = Am^4N^{-1}\phi(\omega)E^{\pm}(m, \omega)E(m), \qquad (2)$$

with $A = 0.10$ and

$$\phi(\omega) = [(\omega^2 - f^2)/(N^2 - \omega^2)]^{1/2}.$$

Representation (2) has been constructed with two properties in mind. The first is that the transport $F(m_c)$ [$= \int_f^N F(m_c, \omega)\, d\omega$] is consistent with the model validation study presented in Polzin et al. (1995): $(1 - R_f)F(m_c)$ accurately predicts the rate of dissipation of turbulent kinetic energy ϵ to within a factor of 2 [R_f, the flux Richardson number, expresses the partitioning of turbulent production into potential energy fluxes and dissipation ($R_f \cong 0.2$)]. The second property is that (2) represents a relaxation principle that will tend to produce a white shear spectrum $E_k \propto m^{-2}$, with E_k being the vertical wavenumber kinetic energy spectrum.

The intended domain of applicability of the closures F and G is $m < m_c$, where m_c is a high wavenumber cutoff in the shear spectrum (Gargett et al. 1981; Duda and Cox 1989) defined by

$$2\int_0^{m_c} m'^2 E_k(m')\, dm' = 0.7N^2. \qquad (3)$$

At higher wavenumber, observed spectra roll off as $E_k \propto m^{-3}$ in response to strong nonlinearity or instability (Polzin 1996) not captured by the flux scheme (2).

Agreement between dissipation measurements and predictions based upon expressions similar to (2) was noted by Polzin et al. (1995) for datasets that exhibited non-GM characteristics. Deviations from the GM spectral model [spectral amplitude, spectral shape in both the vertical wavenumber and frequency domain, anisotropy (nonequal distribution of energy with respect to direction), and inhomogeneity (spatial gradients in N-scaled spectral amplitude)] were cataloged. In order of decreasing importance, the dissipation rate was determined to depend upon N^2, the spectral amplitude, and the average frequency content of the internal wave field. Notably, the dissipation rate appeared to be insensitive (within the factor of 2 uncertainty of the observations) to variations in the shape of the vertical wavenumber spectrum, anisotropy, and inhomogeneity. Thus, use of (2) in the following to examine the spatial evolution of an anisotropic wave field is not a purely speculative extrapolation.

2) THE BOTTOM BOUNDARY CONDITION

Estimates of the energy spectra $E^{\pm}$ and the vertical profile of turbulent dissipation $(1 - R_f)F(m_c)$ can be obtained by solving (1) given boundary conditions on the energy spectrum. The boundary conditions at the bottom and surface for the upward- and downward-propagating waves are, respectively,

$$C_{gz}E^{+} = C_{gz}\Phi(E^{-}) + E_{\text{source}}(m, \omega, z = 0) \quad \text{and} \quad (4)$$

$$C_{gz}E^{-} = C_{gz}E^{+} - E_{\text{source}}(m, \omega, z = H), \qquad (5)$$

where $\Phi(E^{-})$ represents a scattering transform (e.g., Müller and Xu 1992) and E_{source} is prescribed by models of internal wave generation at the bottom ($z = 0$) and the surface ($z = H$).

b. Simplifying assumptions

1) THE RADIATION BALANCE EQUATION

The intent here is to simplify the evolution equation (1) sufficiently that it can be solved analytically, with the express intent of understanding the processes that affect the magnitude and structure of the dissipation profile. First, the focus is upon steady-state solutions; that is, $\partial_t E^{\pm} = 0$. Second, only the case of constant stratification is examined below. Inclusion of the backscattering term on the right-hand-side of (1) stymied analytic progress in the variable N case. Third, (1) is integrated over the frequency domain, $\int_f^N (1)\, d\omega$, with no-flux boundary conditions of $G(m, \omega = f) = G(m, \omega = N) = 0$. An intermediate expression for the energy balance results:

$$\pm\frac{\partial\left[\int_f^N C_{gz}(m,\omega)E^{\pm}(m,\omega)\,d\omega\right]}{\partial z}+\frac{\partial F^{\pm}(m)}{\partial m}=\frac{1}{2m}[F^{\mp}(m)-F^{\pm}(m)]+\frac{1}{2}\int_f^N\frac{(G^{\mp}-G^{\pm})}{\varphi}\frac{\partial\varphi}{\partial\omega}\,d\omega.$$

Further simplification is possible. The factor $\varphi=[(\omega^2-f^2)/\omega^2(N^2-\omega^2)]^{1/2}$ and is independent of ω in the limit $f\ll\omega\ll N$. Thus, in the hydrostatic-nonrotating regime, $\partial_\omega\varphi=0$ and the evolution of the energy spectrum is independent of G. Note also that the frequency dependence of C_{gz} matches that of ϕ in the hydrostatic-nonrotating regime. [The same linear dependence of F upon ω also characterizes the diffusive representation for F derived in McComas and Bretherton (1977).] Solutions to (1) in this regime are therefore independent of frequency. In particular, solutions for a broad-frequency-band wave field are identical to narrow-frequency-band solutions for which $E(\omega)=\delta(\omega-\tilde{\omega})$, where the frequency $\tilde{\omega}$ is identified as a weighted average: $\tilde{\omega}=\int_f^N\omega' E(\omega')\,d\omega'$. This narrowband representation is invoked and backscattering associated with frequency domain transfers neglected below. In the following, ω should be regarded as an average frequency.

These assumptions define a pair of coupled, nonlinear partial differential equations governing the vertical evolution of the vertical wavenumber spectrum:

$$+\frac{\partial E^+(m)}{\partial z}+\frac{A\beta(\omega)m}{N^2}\frac{\partial\{m^4E^+(m)[E^+(m)+E^-(m)]\}}{\partial m}=\frac{A\beta(\omega)m^4}{2N^2}[E^-(m)-E^+(m)][E^+(m)+E^-(m)] \quad (6)$$

and

$$-\frac{\partial E^-(m)}{\partial z}+\frac{A\beta(\omega)m}{N^2}\frac{\partial\{m^4E^-(m)[E^+(m)+E^-(m)]\}}{\partial m}=\frac{A\beta(\omega)m^4}{2N^2}[E^+(m)-E^-(m)][E^+(m)+E^-(m)]. \quad (7)$$

The factor $\beta(\omega)=\omega(N^2-f^2)/[(\omega^2-f^2)(N^2-\omega^2)^3]^{1/2}$ attains its minimum value of 1.0 in the limit $f^2\ll\omega^2\ll N^2$. Given the closure scheme presented in (2), rotation diminishes the vertical flux of energy in relation to the downscale transfer of energy so that wave energy is trapped closer to its source. For nonhydrostatic waves, (2) implies that downscale fluxes increase more rapidly than the rate of increase of vertical energy flux with wave frequency so that nonhydrostatic waves are again dissipated closer to their source. Absent rotational and nonhydrostatic effects, $\beta(\omega)=1.0$, and (6)–(7) state that the vertical evolution of the vertical wavenumber energy spectrum is independent of wave frequency. Thus, within the hydrostatic and nonrotating limits, the evolution of vertical wavenumber spectra of narrow- and broad-frequency-band internal wave fields will be identical.

2) The bottom boundary condition

In a linear problem, one obtains solutions to the differential equation and then these solutions are summed to meet specific boundary conditions. That approach will not work for this nonlinear problem. In order to make progress, the bottom boundary condition (4) will be simplified to match the interior solutions:

$$E_{\text{source}}(m,\omega)=C_{gz}(m,\omega)[E^+(m,\omega,z=0)-E^-(m,\omega,z=0)]. \quad (8)$$

Physically, the downgoing wave field is assumed to reflect as from a flat bottom, for which $\Phi(E^-)=E^-$.

3. Idealized solutions

The effort below is to find solutions to the idealized equation set (6) and (7) representing the vertical evolution of the finescale internal wave field.

a. Uncoupled solutions

The coupling between upward- and downward-propagating fields through the right-hand side of (6) and (7) adds considerable complexity to the analysis. It is instructive to consider solutions to the energy balance that neglect these terms. Note, however, that these solutions do not conserve momentum. Without the backscattering term, (6) becomes

$$\frac{\partial E(m)}{\partial z}+\frac{A\beta(\omega)m}{N^2}\frac{\partial[m^4E^2(m)]}{\partial m}=0, \quad (9)$$

in which $E=E^+$ represents a unidirectional field propagating away from the bottom boundary.

A solution to (9) can be found by the separation of variables, specifying that only the amplitude, not the shape, of the vertical wavenumber spectrum evolves with distance from the bottom boundary:

$$E(m,z)=\frac{1}{1+4A\beta(\omega)N^{-2}bm_0^4z}\frac{bm_0^2}{m^2}\left(1-\frac{m_0^2}{m^2}\right). \quad (10)$$

The solution has two characteristic parameters: m_0 rep-

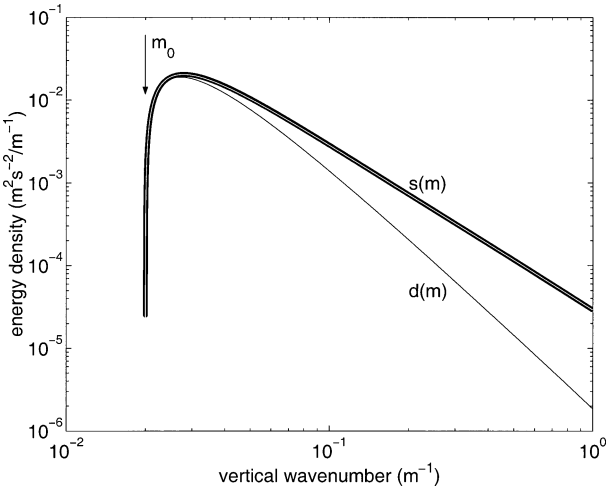

FIG. 2. Typical energy spectra for the sum [$s(m)$, thick] and difference [$d(m)$, thin] functions. The unidirectional solution (10) is overplotted on the sum spectrum as a white line. The parameters are those of the observed spectrum: $m_0 = 0.02\ \mathrm{m}^{-1}$, $c_1 = c_2 = 5.4 \times 10^{-8}$, $N = 1 \times 10^{-3}\ \mathrm{s}^{-1}$, and $A = 0.1$.

resents the low-wavenumber limit of a bandwidth-limited spectrum and b is a spectral amplitude. Note that bm_0^2 can be directly interpreted as the level of the gradient spectrum $m^2E(m)$, $bm_0^2 \cong m^2E(m \gg m_0, z = 0)$.

The solution exhibits the GM spectral dependence of m^{-2} at high wavenumber (Fig. 2). Such solutions have the property that the rate of energy transfer to smaller scales, $F(m)$, is approximately independent of m at high wavenumber. Physically, m_c (3) represents the limit of validity for (2). At higher wavenumber, observed spectra roll off as approximately $E(m) \propto m^{-3}$. At these scales, the downscale transfer of energy may be dominated by processes other than wave–wave interactions. In particular, shear instability (Polzin 1996) and quasi-permanent finestructure (Polzin et al. 2003) may shape the spectrum. Significantly, these finescale processes are too large to be classified as 3D turbulence. Thus, the solutions determined here do not link continuously in the vertical wavenumber domain to the inertial subrange of 3D turbulence. The rate of dissipation of turbulent kinetic energy ϵ, however, can be defined in terms of the downscale flux $F(m)$ in the limit as $m \to \infty$:

$$\epsilon = \lim_{m\to\infty} (1 - R_f)F(m) = \frac{(1 - R_f)A\phi(\omega)N^{-1}b^2m_0^4}{[1 + 4A\beta(\omega)N^{-2}bm_0^4z]^2}. \quad (11)$$

Note that the dissipation estimate at the bottom boundary is proportional to the square of the high-wavenumber shear spectrum, consistent with the model validation study presented in Polzin et al. (1995).

With (11), the dissipation scale height $h_\epsilon = -\epsilon(d\epsilon/dz)^{-1}$ is

$$h_\epsilon = \lim_{m\to\infty} -\frac{\epsilon}{d\epsilon/dz} = \frac{N^2}{4A\alpha\beta(\omega)bm_0^4} + \frac{z}{2}, \quad (12)$$

with $\alpha = 2$. Larger spectral amplitude (bm_0^2) implies larger dissipation and smaller scale height at the bottom boundary, which stems from the fact that the decay of wave energy by wave–wave interactions is a nonlinear process. The scale height increases with distance from the bottom boundary. As the spectrum decays in amplitude, wave–wave interactions are weaker and, as a consequence, the transport of energy toward dissipation scales and thus the relative decay of the spectrum with height above bottom are less rapid. The scale height can also be interpreted as the ratio between the vertical energy flux and the downscale energy transport F. For constant high-wavenumber shear spectral density (bm_0^2 = const), smaller m_0 implies both greater internal wave energy and vertical energy flux, while the specification of constant spectral amplitude implies a constant drain of energy to smaller scales. As a consequence, the vertical wavenumber energy spectrum evolves more slowly with distance from the bottom. Last, note that relations (11) and (12) converge rapidly. If, for example, $m_c > 2m_0$, $0.75 < F(m_c)/F(m = \infty) < 1.0$.

b. Coupled solutions

The coupled (momentum conserving) solution is approached by assuming the sum ($E^+ + E^-$) and difference ($E^+ - E^-$) spectra are separable. With [$E^+ + E^- \equiv S(z)s(m)$] and [$E^+ - E^- \equiv D(z)d(m)$], manipulation of (6) and (7) returns

$$\frac{\partial}{\partial z}\left[\frac{N^2}{A\beta}D(z)\right] + c_1S^2(z) = 0, \quad (13)$$

$$m\frac{\partial}{\partial m}[m^4s^2(m)] = c_1d(m), \quad (14)$$

$$\frac{\partial}{\partial z}\left[\frac{N^2}{A\beta}S(z)\right] + c_2S(z)D(z) = 0, \quad \text{and} \quad (15)$$

$$\frac{\partial}{\partial m}[m^5s(m)d(m)] = c_2s(m). \quad (16)$$

The factors c_1 and c_2 are the separation constants.

The vertical structure equations (13) and (15) can be combined to obtain a second-order nonlinear equation for $D(z)$:

$$D''(z) + \frac{2c_2A\beta}{N^2}D(z)D'(z) = 0. \quad (17)$$

This equation can be solved by noting that (i) it is ''exact,'' and integration returns a Ricatti equation; (ii) the Ricatti equation can be transformed into a Bernoulli equation with the substitution $D(z) = \hat{D}(z) + c_3$, where c_3 is proportional to the integration constant obtained from (i); and (iii) transforming the Bernoulli equation for $\hat{D}(z)$ into a first-order, linear equation [e.g., Bender and Orzag (1978) sections 1.5 and 1.6]. Two distinct sets of solutions result from this manipulation.

1) REFLECTING UPPER BOUNDARY

The first set of solutions is appropriate for a bounded ocean with upper surface at $z = H$. After applying boundary conditions of $D(z = H) = 0$ (i.e., perfect reflection at the upper boundary) and $C_{gz}d(m)D(z = 0) = E_{\text{source}}$ (planar reflection of the downward-propagating wave field plus an energy source E_{source} at the bottom boundary) one obtains

$$D(z) = -\gamma \tan[\gamma(z - H)] \quad \text{and}$$
$$S(z) = \gamma/\cos[\gamma(z - H)]. \tag{18}$$

The coefficient γ is then determined as the smallest eigenvalue, and the amplitude of the spectrum is set by equating the difference spectrum with a source spectrum. These solutions address the depth-integrated energy balance for an ocean with constant stratification. In the variable stratification of the ocean, decreasing vertical wavelength associated with wave propagation into increasing stratification will couple with nonlinearity to efficiently transport energy from large to small scales. As this effect is not represented in the flux law (2), further attention is restricted to the abyssal, near-bottom decay process for which changes in stratification are negligible.

2) UNBOUNDED DOMAIN

The near-field decay is described by a second set of solutions. These are obtained by setting $c_3 = 0$ and represent an unbounded ocean. The bottom-boundary condition is $C_{gz}d(m)D(z = 0) = E_{\text{source}}$, and the solution is required to decay with height:

$$D(z) = S(z) = \frac{1}{1 + z/z_o}, \tag{19}$$

with $z_o = N^2/c_1A\beta = N^2/c_2A\beta$ so that $c_1 = c_2$.

The structure in the vertical wavenumber domain can be determined numerically. After specifying c_1 and c_2, the coupled system of (14) and (16) was solved using a Runge–Kutta scheme subject to initial conditions of $d(m_0) \ll s(m_0) \ll s(2m_0)$. This implies initial conditions on the gradients at m_0. The resulting solutions are not sensitive to these initial conditions as long as they are sensibly consistent with the uncoupled solution (10). The resulting vertical wavenumber spectra are bandwidth limited and rise steeply to a peak (Fig. 2). The sum solution $s(m)$ then falls off with a power law of $s(m) \propto m^{-2}$. The difference solution $d(m)$ falls off somewhat more steeply.

Examination of the numerical solutions reveals that the sum solution $s(m)$ is quite closely approximated by the uncoupled solution (10),

$$s(m) \cong \frac{bm_0^2}{m^2}\left(1 - \frac{m_0^2}{m^2}\right), \tag{20}$$

(Fig. 2) and that

$$z_o^{-1} = 2A\alpha\beta(\omega)N^{-2}bm_0^4. \tag{21}$$

For the numerical solutions discussed below, $\alpha = 2.31$ to within 1%. Comparison of (19)–(21) with (10) shows that the effect of backscattering is to decrease the decay scale z_o by about 15%. Use of the approximate results (20) and (21) is made next in examining the parameter dependence of the solutions.

c. Parameter dependence

The parameter dependence of the dissipation and scale height h_ϵ are more intuitively examined in terms of wavenumber m_0 and velocity variance. Under the hydrostatic and nonrotating approximations, $\langle u^2 \rangle \cong 2m_0b/3$ and $\beta(\omega) = 1.0$. With $R_f = 0.2$, the dissipation and scale height at $z = 0$ using (20) and (21) are

$$\epsilon|_{z=0} \cong 0.18\omega m_0^2\langle u^2\rangle^2/N^2 \quad \text{and}$$
$$h_\epsilon|_{z=0} \cong 0.72N^2/m_0^3\langle u^2\rangle. \tag{22}$$

This dissipation rate is more sensitive to variation in rms velocity than peak wavenumber (Fig. 3), demonstrating the dependence of ϵ upon spectral level rather than peak wavenumber. Given the quadratic scaling of the dissipation rate with spectral level, a factor-of-2 increase in rms velocity implies a 16-fold increase in dissipation. The scale height exhibits a greater dependence upon the peak wavenumber, m_0, than the dissipation rate (Fig. 3), because the energy flux is determined by the largest scales. Profiles of turbulent diffusivity,

$$\kappa_\rho = \frac{R_f F(m = \infty)}{N^2} = \frac{0.2A\omega(bm_0^2)^2/N^4}{(1 + 2A\alpha N^{-2}bm_0^4z)^2}, \tag{23}$$

exhibit the same parameter sensitivity as ϵ (Fig. 4).

Several broad conclusions can be drawn from Figs. 3 and 4. First, given the sensitivity of the magnitude and vertical variability of turbulent dissipation apparent in the model and variability in topographic roughness, barotropic tides, and mesoscale eddy velocities that determine $\langle u^2 \rangle$, and m_0 at the bottom boundary, no single answer is available to prescribe the vertical profile of turbulent diffusivity. Second, the problem of enhanced mixing in the near-bottom region over rough bathymetry (Polzin et al. 1997) is not directly associated with the generation of large-vertical-wavelength internal waves. Data from the Brazil Basin (section 4) exhibit bottom dissipations $O(1 \times 10^{-8})$ W kg^{-1} and decay scales of approximately 150 m. Such dissipation requires a shear spectral level at high wavenumber an order of magnitude larger than the GM model ($2m^2E_k = 7N^2/2\pi$). The rapid decay of dissipation with increasing height above bottom necessitates a rapid decay of shear or, equivalent, spectral level at high wavenumber. This is possible here only if the shear spectrum is bandwidth limited to high wavenumbers. For example, specifying the peak wavenumber as the GM mode scale [$m_0 = (\pi j_*/1300 \text{ m})(N/3 \text{ cph})$ with $j_* = 3$ (implying mode 3)] returns dissi-

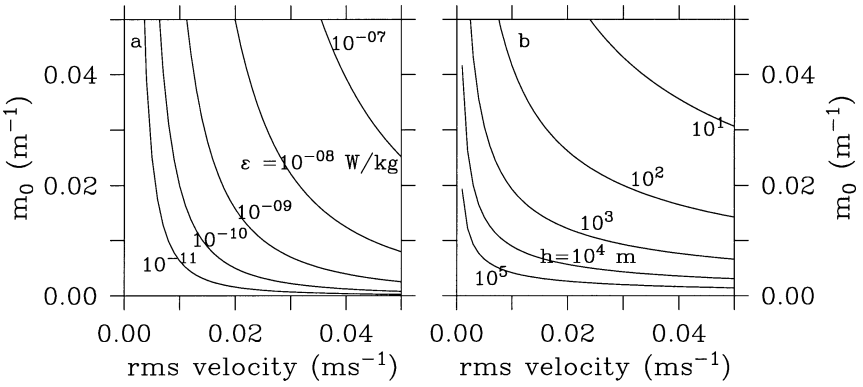

FIG. 3. Contours of (a) dissipation and (b) dissipation scale height at the bottom boundary estimated from (19). The buoyancy frequency is specified as $N = 1 \times 10^{-3}\ s^{-1}$, and $\omega = 1.4025 \times 10^{-4}\ s^{-1}$. The velocity variance was determined from the sum spectrum $s(m)$ rather than the difference $d(m)$.

pation scale heights in excess of 10^4 m at $N = 1 \times 10^{-3}\ s^{-1}$ even if the spectral level is taken to be 10 times the GM specification. A low-mode tide may, indeed, result from the generation process. Considered in isolation from the high-wavenumber response, though, a large vertical-wavelength tide will have little shear and will support only weak mixing.

4. A comparison

Despite the highly idealized nature of the solutions discussed above, quantitative agreement can be found between these solutions and dissipation data presented in Polzin et al. (1997) (Fig. 5). A reasonable fit of $\epsilon = \epsilon_0/(1 + z/z_0)^2$ to the observed dissipation data can be

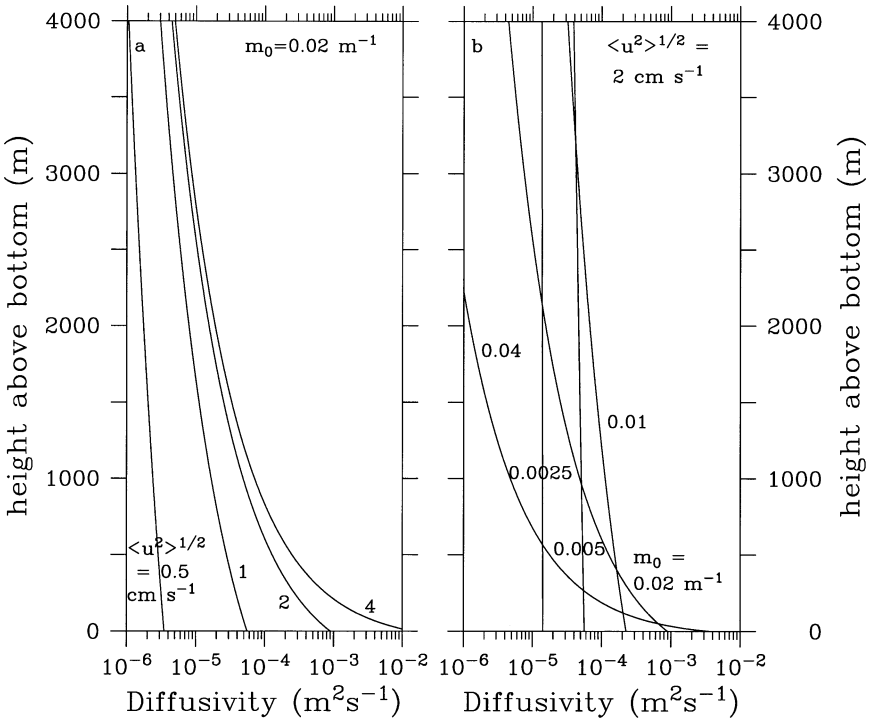

FIG. 4. Vertical profiles of turbulent diffusivity estimated from (20) for (a) constant peak wavenumber, $m_0 = 0.02\ m^{-1}$, as a function of rms velocity $\langle u^2 \rangle^{1/2}$ of the difference spectrum $d(m)$ and (b) constant rms velocity, $\langle u^2 \rangle^{1/2} = 2$ cm s^{-1}, as a function of peak wavenumber, m_0. The buoyancy frequency is specified as $N = 1 \times 10^{-3}\ s^{-1}$, and $\omega = 1.4025 \times 10^{-4}\ s^{-1}$. The frequency parameter $\beta(\omega) = 1.0$, which is equivalent to invoking the hydrostatic, nonrotating limit.

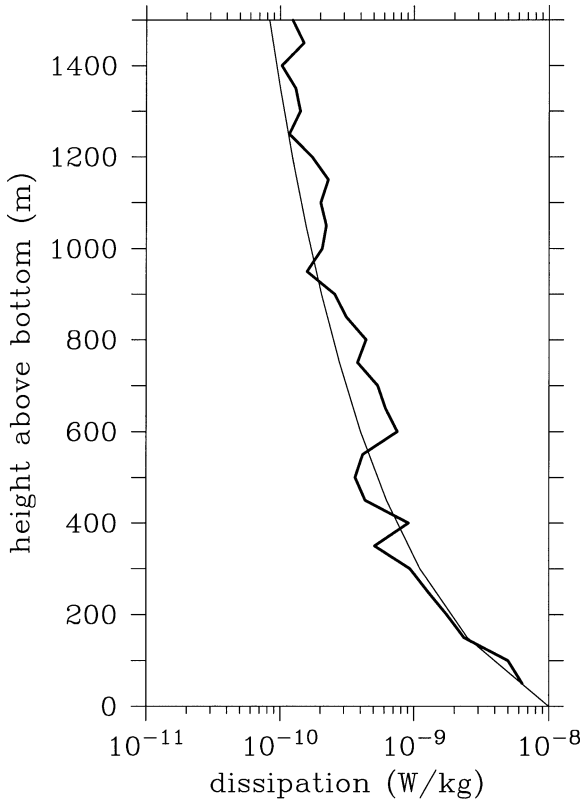

FIG. 5. Dissipation vs height above bottom over rough bathymetry in the Brazil Basin. The dissipation data represent an average over the 30 stations that appear in Fig. 3 and east of 18°W in Fig. 2 of Polzin et al. (1997). The thin line represents a fit to the data. The average buoyancy frequency profile decreases weakly with height above bottom, with $N = 1 \times 10^{-3}$ s^{-1} to within ±30%.

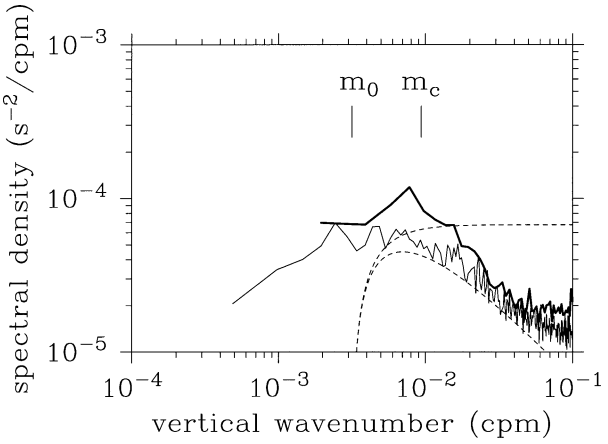

FIG. 6. Shear spectra corresponding to the dissipation data in Fig. 5. The spectra are estimated using piece lengths of 512 (thick, solid) and 2048 m (thin). In both cases the transform interval starts at a height above bottom of 100 m. The spectrum with a piece length of 512 m thus represents conditions closer to the bottom boundary. Overplotted is the idealized solution for the sum and difference shear spectra (dashed lines; see Fig. 2). The idealized spectra have been given their average amplitude corresponding to a height above bottom of 100–612 m. The cutoff wavenumber of the observed near-boundary spectrum m_c and the low-wavenumber roll off of the idealized solutions m_0 are delineated above the data.

obtained with $\epsilon_0 = 1 \times 10^{-8}$ W kg^{-1} and $z_0 = 150$ m. The relations (11) and (21) return a model spectral level $bm_0^2 = 2.9 \times 10^{-5}$ s^{-2} m and vertical wavelength $2\pi/m_0 = 315$ m for $\omega = 1.4025 \times 10^{-4}$ s^{-1} (an M_2 semidiurnal internal tide), $R_f = 0.2$, $A = 0.10$, $N = 1 \times 10^{-3}$ s^{-1}, and $f = -0.53 \times 10^{-4}$ s^{-1}. The observed shear spectra (Fig. 6) exhibit the following salient features: (i) The near-boundary spectrum is peaked at approximately $\lambda_v = 130$ m. This peak is close to $m_c = 9.4 \times 10^{-3}$ cpm (3). (ii) The shear spectrum for wavenumbers $m < m_c$ relaxes with height above bottom to a power law (m^0 in shear and m^{-2} in energy) consistent with the flux representation (2). The observed spectra exhibit a steeper roll off at high wavenumber and more energy at low wavenumber than the solutions discussed above. The high-wavenumber roll off likely occurs in response to strong nonlinearity for vertical wavenumber $m > m_c$ (3), which is not described by the flux law (2).

The enhanced energy content at low wavenumber evident in the data is believed to be associated with the wave generation process. The consequence of neglecting this low-wavenumber energy is that an estimate of the dissipation based upon the idealized solutions will be biased low for large z. Given its relatively low wavenumber content, the neglected energy is likely to be dissipated in or near the thermocline where the observations indicate $K \cong (0.1\text{–}0.2) \times 10^{-4}$ m^2 s^{-1}. The energy source associated with the model parameters is $E_{\text{source}} = 1.9$ mW m^{-2}, or about one-half of that inferred from the observed depth-integrated dissipation record, $(1 - R_f)^{-1} \int_0^H \epsilon\, dz = 3.7$ mW m^{-2}. The difference between the energy flux estimate and the depth-integrated dissipation is dominated by thermocline contributions.

Turbulent dissipation is associated with enhanced wave shear more so than enhanced wave velocity. The idealized solutions associate large dissipations ($\epsilon = 1 \times 10^{-8}$ W kg^{-1}) noted in the Brazil Basin data with velocities of $U_{\text{rms}} = 2.55$ cm s^{-1} and $U_{\text{rms}} = 3.6$ cm s^{-1} for the difference and sum wave fields, respectively. These are similar to the GM model at low stratification ($N = 1 \times 10^{-3}$ s^{-1}). The wave shear at the bottom boundary, on the other hand, is 20 times the shear in the GM spectrum. The difference depends entirely on how that 3 cm s^{-1} is distributed in the vertical-wavenumber domain.

The idealized solutions depict the decay of a bandwidth-limited finescale internal wave field propagating away from the bottom boundary. This appears to be a reasonable description of near-bottom observations obtained above rough bathymetry in the Brazil Basin. The bottom boundary condition $C_{gz}d(m)D(z = 0) = E_{\text{source}}$ equates the difference spectrum with a source function (E_{source}) for the internal wave field. Hitherto it has been assumed that these two are consistent. Relationships between the difference spectrum and extant models of

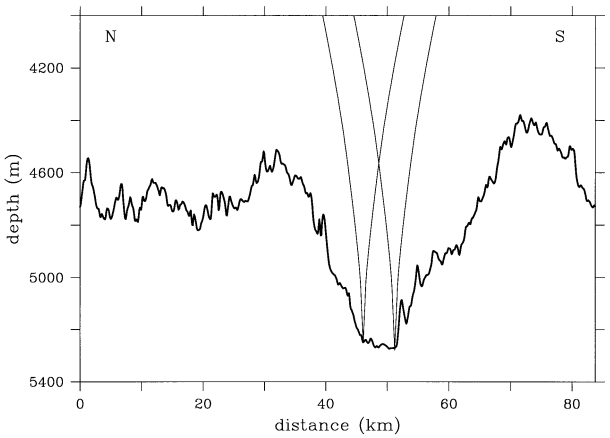

FIG. 7. A north–south section of bathymetry from the Brazil Basin along a line extending from 21°15′S, 18°28.215′W to 22°00′S, 18°21.605′W. The data were obtained with a multibeam system. Thin lines denote the ray characteristics of the semidiurnal tide and were estimated using the observed density profile. The segment from 20 to 55 km corresponds to Fig. 3 of Polzin et al. (1997).

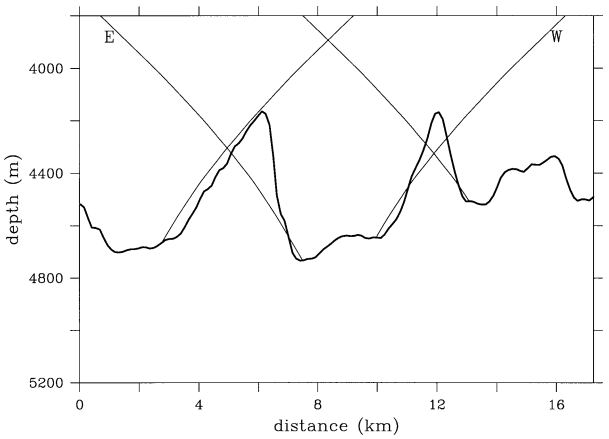

FIG. 8. An east–west section of multibeam bathymetry along 21°12.5′S from 18°30.00′ to 18°40.00′W. Internal wave ray characteristics, estimated using the observed density profile, are shown as thin lines. This section is approximately aligned with the direction of steepest ascent/descent. Note the asymmetric nature of the topography. These data correspond to the roughness elements in Fig. 2 of Polzin et al. (1997).

wave generation and scattering are briefly considered in the next section.

5. An interpretation in terms of extant models of wave generation and scattering

a. Midocean ridge bathymetry

Midocean ridge bathymetry is highly complex. The ridge crest represents the boundary between two plates moving in opposing directions. New crust is being formed at these spreading centers. In the case of the South Atlantic, the ridge is cut by offset fractures, which are evident as rectilinear canyons running normal to the ridge crest and extending across the entire ridge. Midocean ridges are also textured with abyssal hills. Abyssal hills are understood to be formed by faulting and volcanism at the ridge crest. Their morphology is believed to depend upon basin-scale attributes of ridge processes such as spreading rates and elastic thickness of the lithosphere adjacent to the ridge axis; see, for example, Goff (1991).

Abyssal hills make the dominant contribution to the topographic slope in the Brazil Basin. The slope of the Mid-Atlantic Ridge itself is quite small, rising 3000 m (generously) over 1500 km (slope = 0.002). Canyons associated with offset fractures (Fig. 7) are obvious features on global topographic charts, but again have a relatively small slope (relative depth change/half-width = 800 m/20 km = 0.04) and are spatially isolated features. In comparison, internal tide characteristics are steeper (Fig. 7). Abyssal hills (Fig. 8) have similar height variations as canyons, but these occur over smaller horizontal scales, so that typical slopes are much larger (relative depth change/half-width = 400 m/2 km = 0.2) and can exceed those of the ray characteristics. And as opposed to being isolated like offset fractures, abyssal hills are ubiquitous features, filling in the areas in between the offset fractures. They are not well represented in global topographic datasets [e.g., General Bathymetric Chart of the Oceans (GEBCO), ETOPO, or Smith and Sandwell (1997)] as a multibeam echosounding system is required to sample such small scales and multibeam coverage of the world's ocean is spotty.

The topography depicted in Fig. 8 is crudely consistent with published statistical descriptions of abyssal hills (Goff 1992) in the South Atlantic. Rms heights of 200 m and a distance between peaks of 6–10 km are typical. Moreover, such analyses suggest the abyssal hills are anisotropic and asymmetric. The hills are anisotropic in the sense that faults are typically parallel to the ridge axis and result in larger spatial scales in that direction. In Figs. 7 and 8, the short scales are oriented virtually east–west and the long scales run north–south. (The topography depicted in Fig. 7 lies along a series of abyssal hill crests.) The hills in Fig. 8 are asymmetric as their east-facing slopes are typically steeper than the west-facing slopes. Such asymmetry can be interpreted in terms of the faulting process (e.g., Goff 1991). The hills are additionally asymmetric in that the peaks tend to be taller than the troughs are deep. In terms of a Fourier decomposition, such asymmetry translates into increased small-scale variance.

A convenient description of abyssal hills is contained within an anisotropic parametric representation of the topographic spectrum $H(k, l)$ [Goff and Jordan (1988)]:

$$H(k, l) = \frac{4\pi\nu h_o^2}{l_o k_o (k^2/k_o^2 + l^2/l_o^2 + 1.0)^{(\nu+1)}}, \qquad (24)$$

where k_o and l_o are roll-off wavenumbers, ν prescribes a high-wavenumber power law, and h_o is the rms height. The work below utilizes values for the Mid-Atlantic

Ridge at 26°S ($k_o = 1.5 \times 10^{-4}$ m^{-1}, $l_o = 5.4 \times 10^{-4}$ m^{-1}, $h_o = 210$ m, and $\nu = 0.86$) obtained from tables in Goff (1991).

The intent below is to consider how extant models of internal wave generation and scattering can be used to translate the spectral content of such topography into the observed peaked internal wave shear spectrum (Fig. 6).

b. Wave generation and scattering

1) A QUASI-LINEAR GENERATION MODEL WITH INFINITESIMAL AMPLITUDE TOPOGRAPHY

Barotropic tidal flow (having amplitude U_o) of a stratified fluid over sloping topography induces a vertical velocity that, in turn, represents a forcing of baroclinic motions. If the length scale of the topography ($1/k$) is large relative to the tidal displacments ($U_o/\omega \ll 1/k$), the rms vertical velocity is proportional to the rms topographic slope. If the length scale of the topography is small ($U_o/\omega \gg 1/k$, representing the advective limit), the rms vertical velocity is proportional to the rms topographic height.

A representation of the forced response in both limits can be obtained by including barotropic tidal advection in the momentum equations and the resulting model is referred to as quasi linear. For infinitesimal-amplitude topography, the rate of conversion (Bell 1975) from barotropic to baroclinic motions is

$$E_{\text{source}}(k, l, \omega_n, z = 0, t) = \frac{1}{2\pi^2} n\omega_1[(N^2 - n^2\omega_1^2)(n^2\omega_1^2 - f^2)]^{1/2}(k^2 + l^2)^{-1/2} \times H(k, l) J_n^2\{[(k^2U_o^2 + l^2V_o^2)/\omega_1^2]^{1/2}\}. \quad (25)$$

In (25), E_{source} represents the vertical flux or energy as a 2D horizontal wavenumber spectrum, ω_1 is the fundamental frequency of the barotropic tide (M_2), n an integer such that $n\omega_1 < N$, and $\omega_n = n\omega_1$ represents the nth frequency harmonic. The function J_n is a Bessel function of order n, and the factors U_o and V_o in its argument represent the amplitude of the barotropic tide. Equation (25) was evaluated using (24) and barotropic tidal amplitudes from the TPXO model (Egbert et al. 1994) [$(U_o, V_o) = (2.5, 2.1)$ cm s^{-1} for February 1996 after rotating into a coordinate system aligned with the topography]. Last, (25) was converted to a 1D horizontal spectrum by integrating over the horizontal orientation of the horizontal wave vector and then converted to a vertical wavenumber–frequency spectrum by invoking a dispersion relation (Fig. 9).

Viewed as a transfer function, $J_1(q)$ differentiates for values of $q \ll \pi/2$; thus the internal wave energy density is proportional to the topographic slope. In the advective ($kU_o/\omega \gg 1$, small horizontal scale) limit, the energy density of the internal tide is no longer proportional to the topographic slope, but rather proportional to the amplitude of the topographic perturbations. The roll off of the shear spectrum predicted by (25) (Fig. 9) for vertical wavelengths smaller than about $2\pi U_o/N$ ($\cong$100 m) is a result of this effect. This advective limit is approached as the horizontal excursions of the barotropic tide exceed a significant fraction of the topographic wavelength $kU_o/\omega > 1$. A simplistic interpretation is that tidal advection smoothes scales smaller than the tidal excursion. Linear kinematics relates the ''smoothing scale'' $k^{-1} = U_o/\omega$ to a vertical length scale $m^{-1} > U_o/N$.

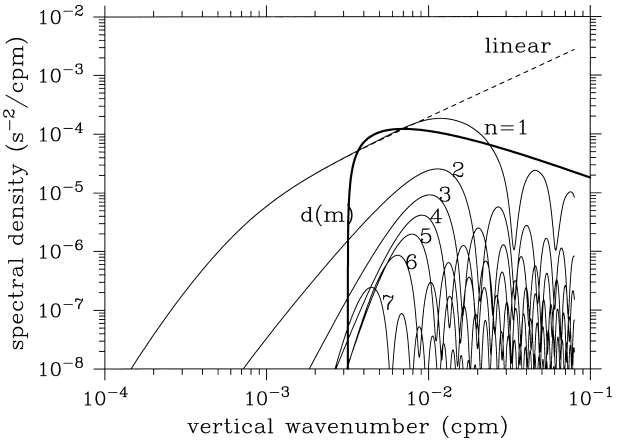

FIG. 9. Shear spectra for the linear internal tide generation model [dashed, (A3)], Bell's quasi-linear model [thin, (25)], and the difference spectrum of the idealized solution (thick, Fig. 2). The frequency-domain harmonics have decreasing amplitude with ascending frequency. The analytic solution has been normalized to its boundary value.

2) LINEAR GENERATION MODELS

Linear models of internal wave generation are addressed in the appendix. The results can be succinctly summarized. Application of a linear generation model to abyssal hill topography is fundamentally flawed. For infinitesimal amplitude topography, a linear model with continuous topography will return the result that the energy in the resulting wave field is proportional to the topographic slope variance. This is rather problematic given the topological character of midocean ridge bathymetry. It can be described as fractal (Goff and Jordan 1988), which implies that the topographic slope variance is unbounded as smaller and smaller scales are included in the slope estimate. The prediction of infinite energy and shear is aphysical because either adiabatic or diabatic nonlinearity will serve to damp the smallest-scale response. Extending a linear model to include finite-amplitude topography only serves to further enhance the predicted wave energy and shear variance.

3) WAVE SCATTERING

Scattering transforms derived by Müller and Xu (1992) and Rubenstein (1988) quantify the spectral

transfers of energy as a downgoing wave reflects from a rough boundary. Such transforms view scattering as a linear process, assume the topographic height to be small relative to the vertical scale of the incident wave, and that the topographic slope is everywhere smaller than the ray characteristic slope. In the limit that the horizontal scales of the topography are much smaller than those of the incident internal wave, the scattering transforms suggest a response proportional to the topographic slope spectrum. Thus, much of the preceding discussion about baroclinic tide generation carries over to the scattering problem. In particular, inclusion of advection in the momentum equations may provide a physical rationale for truncating the topographic slope spectrum, as opposed to the ad hoc truncations invoked in Müller and Xu (1992) and Rubenstein (1988).

c. Interpretation

In interpreting the idealized solutions, there are two tasks. In section 3 it was assumed that the source distribution E_{source} was given by $d(m)$. This relation is, in fact, backward. The difference spectrum should be dictated by the source distribution through (4). The first task is therefore to map the idealized solutions onto the source distribution E_{source}. The second task is to assess the approximate bottom boundary condition (8) for the idealized solutions. For those solutions, the downgoing wave field was assumed to reflect as from a flat bottom; thus, $\Phi(E^-) = E^-$ was invoked.

1) TASK 1: INTERPRETATION OF THE IDEALIZED SOLUTIONS

The interpretive context of this study is that the enhanced finescale velocity variance observed above rough areas of the abyssal Brazil Basin manifests a combination of wave generation and wave scattering that results from bathymetric elements having horizontal scales $\lesssim$1000 m. The idealized solutions presented in section 3 are an attempt to interpret the vertical profile of turbulent dissipation as an end result of the downscale transport of energy associated with nonlinear interactions of this enhanced finescale wave field. They also permit an interpretation of the observed spectrum from the oceanic interior relative to the boundary conditions. It is tempting to identify the peak of the observed shear spectrum with the idealized solutions (Fig. 6) and the peaked shear spectrum of Bell's model with the difference spectrum of the idealized solutions (Fig. 9): better than a factor of 2 agreement in spectral level at the finescale peak is apparent, and the wavenumber of the peak is reasonably well predicted by the barotropic tidal estimates.

With regard to Bell's model, further consideration of the details suggests the following: 1) The peak of the observed shear spectrum occurs at a wavenumber somewhat smaller than N/U_{bt}, where U_{bt} is the rms barotropic tide (2.3 cm s^{-1} here). An alternative might be a smoothing scale $(N/U_{\text{rms}})^{-1}$ with $U_{\text{rms}} > U_{\text{bt}}$ related to the sum of the barotropic tide and the incident wave field. 2) Regardless of the smoothing scale, the bottom energy source estimate using Bell's model ($\sum_{n=1}^{n\omega_1<N} \iint E_{\text{source}}\, dk\, dl = 7.6$ mW m^{-2}) is a factor of 2 larger than that inferred from the observed depth-integrated dissipation, 3.7 mW m^{-2}. Two immediate resolutions of this contradiction come to mind: (i) the topographic spectrum (24) is overestimated and/or (ii) the assumption of a local vertical energy balance is in error. (That is, the excess production propagates horizontally.) The latter is not likely. Müller and Xu (1992) report (albeit on the basis of a linear model) that scattering results in an $O(1)$ transformation of the incident energy flux when the ray trajectories are equal to the topographic slope, as is the case here for the semidiurnal tide (Fig. 8). Since the Brazil Basin experimental site is $O(10)$ bottom bounces from smooth topography, it is doubtful that much internal tide energy escapes regions of rough bathymetry. A scale analysis of the energy equation further supports a local balance (appendix).

Accepting the vertical balance implies that the topography is overestimated by the spectrum (24). But if smaller-amplitude bathymetry is adopted, Bell's model produces an underestimate of the observed near-bottom shear spectrum. This underestimate could, perhaps, be compensated by inclusion of wave scattering effects. A more detailed study is required.

To obtain more detailed ground truthing of the bottom boundary condition could be difficult: The transport of energy to turbulence implies a loss of information and, from the degree of difference between the boundary and interior amplitudes of the idealized solutions (Figs. 6 and 9), the information lost could make it difficult to distinguish differences between model predictions from simple uncertainty in the topographic spectrum.

2) TASK 2: THE APPROXIMATION (8)

The analytic solutions derived in section 3 assume that the backscattered (E^-) wave field reflects from the bottom as if it were flat, $\Phi(E^-) = E^-$ in (8). Little can be concluded on the basis of linear scattering theory for infinitesimal amplitude topography because that approach assumes a perturbation expansion with the vertical wavelength of the incident internal wave much larger than the topographic height $1/m \gg h_o$. This condition is not satisfied over rough bathymetry as $m_0 \cong 0.02$ m^{-1} and $h_o \cong 200$ m.

The fundamental question of how the wavenumber distribution of the downgoing wave field is rearranged upon reflection at the bottom boundary remains. Here we simply note that the downgoing wave field of the idealized solutions carries an energy flux that is small ($\sim$10%) relative to the upgoing waves with $E_{\text{source}} = 1.9$ mW m^{-2}. While the solutions discussed above are en-

ergetically consistent, they represent an idealized situation.

6. Discussion

The long-term goal to which this research contributes is a robust prediction of the vertical profile of turbulent dissipation (and diapycnal diffusivity) from a limited number of input parameters: a spectrum of bottom topography and either barotropic tidal velocity and frequency or mesoscale eddy velocity. The work presented above describes a method for assessing the vertical evolution of a finescale internal wave spectrum originating at the bottom boundary and for diagnosing the resulting vertical profile of turbulent dissipation resulting from wave breaking. In the long term, a more sophisticated numerical treatment of the governing equation is required, as well as the potential revision of the transport laws $F(m, \omega)$ and $G(m, \omega)$. In discussing idealized solutions here, the intent was to explore the sensitivity of the magnitude and vertical structure of turbulent dissipation in response to changes in wave field amplitude, vertical bandwidth, and frequency.

The internal wave field was taken here to be a narrow band process in the frequency domain. This is an ad hoc characterization of the oceanic wave field rather than a limitation of the theory. Yet this characterization is not believed to significantly alter the results presented above as the evolution of the vertical wavenumber spectrum is independent of wave frequency in the hydrostatic and nonrotating limits.

Steady solutions to the governing equation were found. The assumption of a steady balance is clearly an idealization as near-boundary dissipation rates are large enough that the decay time for the total internal wave energy is the same order as the expected temporal variations in the forcing [e.g., a fortnightly period in the case of internal tide generation (Ledwell et al. 2000)].

Of greater concern than the assumption of a steady balance is the treatment of the bottom boundary condition. A downward-propagating wave field associated with either surface sources, reflection of the upward-propagating wave field from the surface, or backscattering of the upward-propagating wave field by nonlinear processes was assumed here to reflect as from a flat bottom. While this bottom boundary condition is energetically consistent, if a rough bottom is an efficient generator of finescale internal waves, one might reasonably expect it to be an efficient scatterer of incident waves as well. The present interpretation of the idealized solutions in terms of wave generation or scattering models is thus problematic.

A further idealization was the assumed constant stratification. In the thermocline, decreasing vertical wavelengths associated with wave propagation into increasing stratification should transport finescale waves to sufficiently small scales where even weak nonlinearity will cause them to dissipate.

Implementing internally consistent boundary conditions with top and bottom boundary sources, allowing for variable stratification, a broad-frequency-band wave field, and time dependence of the source functions at the boundaries, and examining more detailed closure schemes require a more sophisticated numerical technique than employed here and are beyond the scope of this work.

Analytic solutions to the radiation balance equation (1) were obtained for the idealized situation described above. The vertical wavenumber energy spectrum is

$$E(m, z) = \frac{1}{1 + 2\alpha A\beta(\omega)N^{-2}bm_0^4 z}\frac{bm_0^2}{m^2}\left(1 - \frac{m_0^2}{m^2}\right). \quad (26)$$

The spectrum is bandwidth limited to wavenumbers $m > m_0$. The gradient spectrum has an amplitude of $m^2E(m) = bm_0^2$ for wavenumbers $m \gg m_0$ at the bottom, $z = 0$. The corresponding dissipation profile is

$$\epsilon = \frac{\epsilon_0}{(1 + z/z_0)^2}, \quad (27)$$

with

$$\epsilon_0 = (1 - R_f)A\phi(\omega)N^{-1}b^2m_0^4 \quad \text{and}$$

$$z_0^{-1} = 2\alpha A\beta(\omega)N^{-2}bm_0^4.$$

The idealized solutions are not a complete description of the generation and scattering processes: they are too bandwidth limited and, as a consequence, do not capture the entire energy flux associated with the generation process. The ability of the idealized solutions to describe a two-parameter summary of the observed shear spectrum (m_0 and bm_0^2) in terms of a two-parameter summary of the observed dissipation profile (ϵ_0 and z_0) is likely a product of the following two reasons: First, internal-tide generation from rough bathymetry produces a shear spectrum with a peak at vertical wavenumber $m \propto N/U_{\text{bt}}$, where U_{bt} is the amplitude of the barotropic tide. The finescale shear field resulting from internal wave scattering is likely peaked in a similar manner and, arguably, the spectral peak occurs at a vertical wavenumber related to N/U_{rms}, with U_{rms} representing the combined flow due to the barotropic tide and incident wave fields. Second, the flux representation of the spectral transports translates this peak into an abrupt decay of wave energy with height above bottom without reference to larger scales. The robust feature of the idealized solutions is that the peaked character of the observed vertical wavenumber shear spectrum can be mapped onto the idealized solutions. If the idealized solutions make any sense, it is because they capture the initial decay process of a peaked shear spectrum.

The important feature in determining the rapid vertical decay of the dissipation is the presence of a finescale peak having large spectral level. The large spectral level dictates large wave–wave interaction-induced energy transports to small vertical scale and, in turn, large

dissipation rates. This translates into a rapid spatial decay of an enhanced finescale wave field because waves at these scales have a limited ability to propagate vertically. The rapid vertical decay of finescale energy, in turn, implies a rapid decay of turbulent dissipation with height above the bottom. The analysis presented in this paper is an attempt to put this scenario into the simplest possible dynamical framework. This analysis agrees reasonably well with fine- and microstructure data obtained from the Brazil Basin.

Future work will feature more sophisticated numerical treatments of the governing equation along with the specification of the lower boundary condition of $E^{\pm}(m, \omega)$ in terms of wave generation and scattering models. For the purpose of modeling the decay of turbulence as a function of height above bottom, a realistic description will likely need to address the impact of advection in the bottom-boundary condition and finite-amplitude bathymetry on the processes of internal wave generation and scattering. However, such work need not be completed to infer the importance of small-scale bathymetric features. The observed spectral peak corresponds to a horizontal wavelength of $\lambda_h \cong 2\pi U_{\text{bt}}/\omega \cong 1$ km. This horizontal wavelength is smaller than that characterizing the distance between typical abyssal hills (6–10 km). At present, information at these scales is not currently represented in global bathymetric datasets.

Acknowledgments. This work has evolved out of long association with John Toole, Raymond Schmitt, and the High-Resolution Profile Group (Ellyn Montgomery, David Wellwood, and Gwyneth Packard) at the Woods Hole Oceanographic Institution. Their continuing scientific advice and technical support are greatly appreciated. This manuscript was proofread and edited for journal submission by Anne-Marie Michael. Financial support from the National Science Foundation (Grant OCE 94-15589) and the office of Naval Research (Grant N00014097-1-0087) is gratefully acknowledged.

APPENDIX

The 1D Approximation to the Radiation Balance Equation and Three Models of Internal Tide Generation

a. The 1D approximation

St. Laurent and Garrett (2002) interpret these same data in terms of a fundamentally 2D balance. In short, they suggest that less than 30% of the total internal wave energy source at the bottom, which they estimate as 3–5 m W m^{-2}, dissipates near the bottom boundary with the rest assumed to propagate away from the Mid-Atlantic Ridge. Here, the interpretation is 1D and, consequently, all the wave energy input at the bottom boundary is assumed to dissipate locally. The 1D balance is supported by the following scaling for the steady energy balance:

$$\frac{\partial \mathbf{E}_{\text{flux}}}{\partial z} + \frac{\partial \mathbf{E}_{\text{flux}}}{\partial x} = \frac{\epsilon}{1 - R_f} + S_o, \tag{A1}$$

in which $\mathbf{E}_{\text{flux}}(x, z)$ is the energy flux vector, $\mathbf{E}_{\text{flux}} = \int_f^N \int_0^\infty \mathbf{C}_g(m, \omega)E(m, \omega)\, dm\, d\omega$, and $S_o(x)$ is the energy source at the bottom boundary. Assuming that the horizontal length scale (L) of S_o dictates the horizontal length scale of the other variables and that the height scale H is given by vertical variation of ϵ, the ratio of the vertical to horizontal energy flux divergence is

$$\frac{\omega E/mH}{NE/kL} \cong \frac{L\omega}{HN}. \tag{A2}$$

The source S_o varies by an $O(1)$ amount over the entire ridge, which has a half-width of 10°–15° longitude, so $L \sim 1000$ km. In the deep ocean, the stratification is weak ($N/\omega \cong 10$) and the dissipation varies by an $O(1)$ amount over 200 m in height above bottom; thus $H \sim 200$ m. The ratio of the horizontal to vertical flux divergences is thus $O(1/500)$. In the thermocline, $N/\omega \cong 100$ and dissipation varies by an $O(1)$ amount over 500 m. Thus the ratio of horizontal to vertical flux divergences in the thermocline is $O(1/20)$. On this basis, the energy balance is clearly one dimensional.

The justification given by St. Laurent and Garrett (2002) for their partition of the source into local and nonlocal dissipation appears to be an evaluation of wave scattering effects that suggested wave scattering is inefficient. Despite assertions to the contrary, their assessment is qualitatively inconsistant with the scattering transform of Müller and Xu (1992), which results in an $O(1)$ transformation of the incident energy flux when the internal wave ray trajectories are similar to the topographic slope, as is the case for the Mid-Atlantic Ridge.

b. Models of wave generation

1) A LINEAR MODEL WITH INFINITESIMAL AMPLITUDE TOPOGRAPHY

For infinitesimal-amplitude topography, a linear model of internal-tide generation using continuous topography will return the result that the energy density is proportional to the topographic slope variance. This is rather problematic given the topological character of midocean ridge bathymetry. It can be described as fractal (Goff and Jordan 1988), which implies the topographic slope variance is unbounded as smaller and smaller scales are included in the slope estimate. Using a linear model and a continuous representation of midocean ridge bathymetry, the predicted result will have infinite energy density and infinite shear. This is aphysical as either adiabatic or diabatic nonlinearity will serve to damp the smallest-scale response.

One representation of the above comments is a spectral model (Fig. 9) of the internal wave response to oscillatory flow over infinitesimal-amplitude topography:

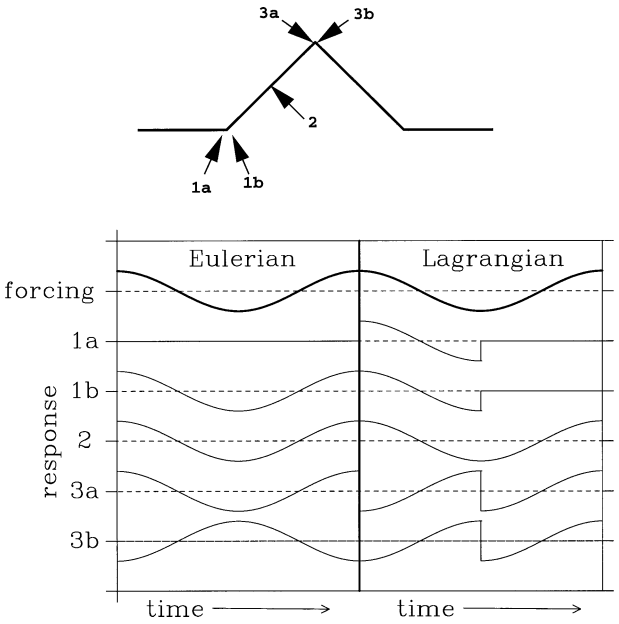

FIG. A1. A schematic representation of the bottom-boundary condition at points 1a, 1b, 2, 3a, and 3b of the triangular planform. Two of the points are close together at the base of the triangle, two are located next to each other but on different sides of the apex, and one is on the middle of the slope. (top) The forcing barotropic velocity is given, and (bottom) the vertical velocity obtained from $w = U_{bt}\partial h/\partial x$ is plotted in both Eulerian and Lagrangian coordinates.

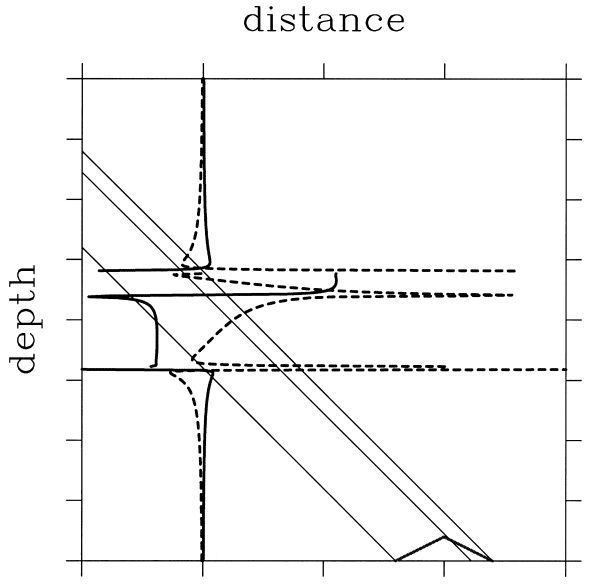

FIG. A2. A linear solution for the triangular bump planform using the method described in Baines (1973). The thin lines to the left of the bump represent ray characteristics. The thick lines represent the real (solid) and imaginary (dashed) parts of the velocity profile. The velocity profiles are discontinuous or sharply peaked where the rays can be traced back to points where the topographic slope is discontinuous. This behavior is characteristic of the solution for infinitesimal-amplitude bathymetry and is consistent with the linear spectral model in Fig. 9.

$$E_{\text{source}}(k, l, \omega, z = 0) = \frac{1}{2\pi^2}\omega[(N^2 - \omega^2)(\omega^2 - f^2)]^{1/2}(k^2 + l^2)^{-1/2} \times H(k, l)[(k^2U_o^2 + l^2V_o^2)/4\omega^2]. \quad \text{(A3)}$$

Here $E_{\text{source}}(k, l, \omega)$ is the horizontal wavenumber–frequency spectrum for the vertical energy flux spectrum, ω is the fundamental frequency of the barotropic tide (M_2), and the factors U_o and V_o represent the amplitude of the barotropic tide.

Apparent in Fig. 9 is a blue shear spectrum that rises with wavenumber as approximately $m^{1.3}$. The corresponding energy spectrum is ''pink,'' tending weakly downward as $m^{-0.7}$. The integrals of both spectra diverge as the upper limit of integration becomes infinite. Thus both predicted wave energy and wave shear are infinite.

Why a linear inviscid model gives rise to a large-amplitude response at small scales is easy to discern. The vertical velocity at the bottom boundary induced by oscillatory flow over sloping topography is proportional to the product of the magnitude of the oscillatory flow and the topographic slope $w[x, z = h(x), t] = U_o(t)\partial h/\partial x$, for example, where h represents the height of a topographic feature. Thus a discontinuity in the topographic slope will induce a discontinuity in the response. Consider an example of the response to flow over a triangular bump (Fig. A1). The time history of the vertical velocity at five positions is shown, as is the forcing oscillatory flow. Adjacent sites exhibit different time histories of vertical velocity where the topography is piecewise continuous, and it should be relatively apparent that these differences will translate into spatial discontinuities in the induced flow field (Fig. A2).

This example represents the fundamental limitation of the bottom boundary condition in a linear model. A linear model is not a physically realistic representation of internal tide generation from midocean ridge topography as its predicted flow fundamentally contradicts its adiabatic premise. While the triangular bump is an idealized description of bathymetry superimposed upon midocean ridges (Fig. 8), it cannot be dismissed as irrelevant because of the abrupt changes in slope. The spectrum of the triangular planform has a high-wavenumber power law of k^{-4}. Observed midocean ridge bathymetry (24) is somewhat *rougher* with a high-wavenumber power law of $(k^2 + l^2)^{-3/2}$ to $(k^2 + l^2)^{-1}$ for $(k^2 + l^2)^{1/2} > l_o$ [cf. (24)].

2) THE QUASI-LINEAR REPRESENTATION OF BELL (1975)

Quite a different picture of the bottom boundary condition is obtained following a water parcel moving with the imposed flow field. Consider prescribing the vertical velocity at the bottom boundary as

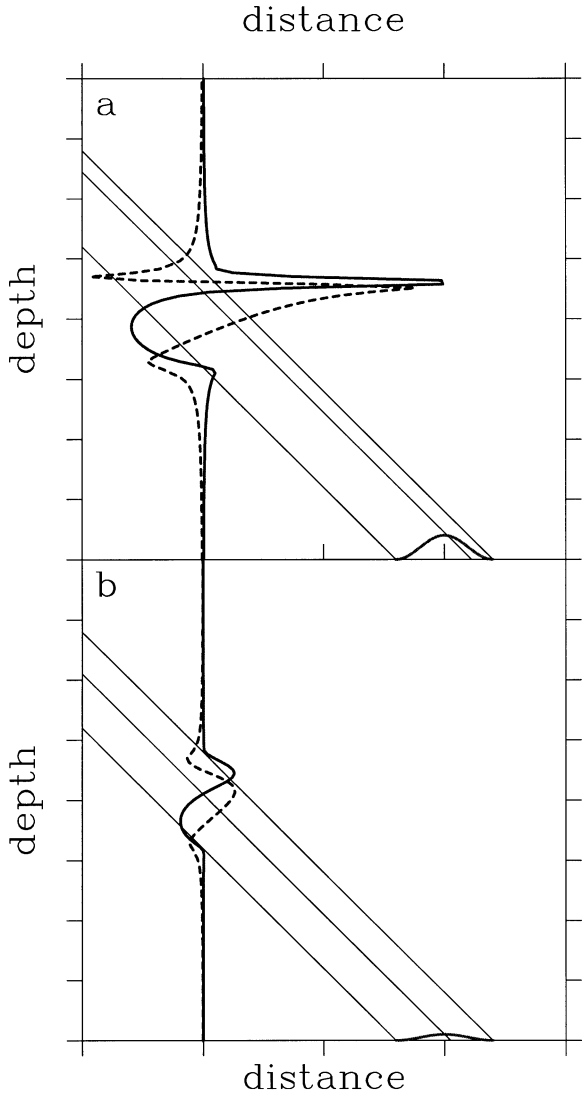

FIG. A3. Linear solutions for a cosine-squared planform. The curvature of this topographic planform is piecewise continuous; thus the velocity profiles are well behaved. Note that the ray tubes emanating from the far side of the topography are compressed and result in enhanced shear as the topographic height increases.

$$w = w\left\{x(t) = x_o + \int_0^t U_o(t')\,dt',\ z = h[x(t)],\ t\right\}$$
$$= U_o(t)\partial h[x(t)]/\partial x.$$

Neighboring points now have similar time histories of vertical velocity (Fig. A1). The spatial domain discontinuities in the Eulerian formulation of the bottom boundary condition have been transferred to the time domain in the Lagrangian framework. Energy and shear variance are consequently finite. The discontinuities in the time domain are described as a sum of harmonics in the frequency domain (25).

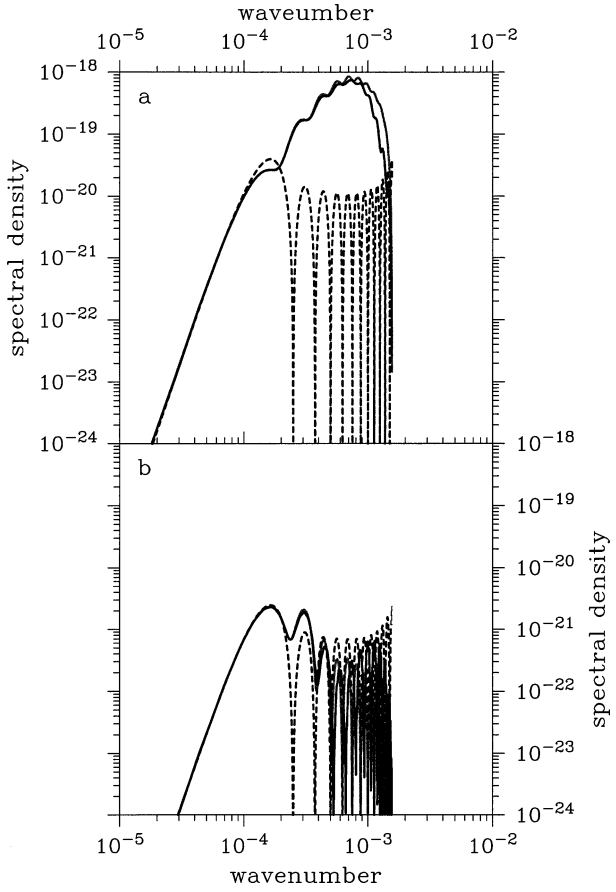

FIG. A4. Spectra of the velocity profiles (solid lines) estimated from an FFT procedure. The dashed line represents the topographic slope spectrum. All spectra have additionally been multiplied by wavenumber to the fourth power (k^4) so that the roll off of the linear, infinitesimal-amplitude solution is white; (a) and (b) correspond to the identical panels in the previous figure.

3) A LINEAR MODEL WITH FINITE-AMPLITUDE TOPOGRAPHY

Bell's Lagrangian formulation of the bottom boundary condition, however, is not a panacea as it assumes the bathymetry to be of infinitesimal amplitude. That is, the condition of no-flow through the bottom boundary is applied at $z = 0$ rather than the bottom boundary $z = h(x, y)$. Baines (1973) discusses a method for solving the linear generation problem subject to the application of the bottom boundary condition at $z = h$. That method utilizes the fact that waves propagate along characteristic paths. For the small-amplitude bathymetry in Fig. A3b, the characteristics emanating from the peak and lower edge of the topography are evenly spaced. As the topography increases in height (Fig. A3a), the wave amplitude increases, and the characteristics coming from the peak and far side contract, with the implication that the wave shear increases. A spectral decomposition (Fig. A4) reveals that the Baines solution is proportional to the topographic slope spectrum when

the topographic height is small. This result also applies at low wavenumber as the topographic height increases. However, there is a range of wavenumbers for which the solution is enhanced and the shear spectrum is peaked. This range of wavenumbers corresponds roughly with $1/L < k < 1/(L - h_o/\vartheta)$, where L is the half-width of the topography, h_o the height, and ϑ the ray characteristic slope. The ratio $h_o/L\vartheta$ represents the relative contraction of ray characteristics from the topographic peak and the far side of the bump as h_o increases.

Contrast the better than factor of 2 agreement between the observed shear spectral peak, the level of the idealized solution (Fig. 6), the idealized solution's difference spectrum, and Bell's quasi-linear, infinitesimal amplitude model prediction (Fig. 9) with the two order-of-magnitude enhancement of shear associated with the finite-amplitude bottom boundary condition (Fig. A4). This degree of shear enhancement is not apparent in the observed spectra, nor is it consistent with the observed dissipation profile. The Baines model using the finite-amplitude bottom boundary condition returns a prediction that is clearly not present in the data. Such an inference from this simple calculation is easily criticized. Major shortcomings include 1) the bathymetry is 3D and the model is restricted by its nature to being 2D, 2) the topographic planform is much smoother than the oceanic topography, and 3) the bathymetry is possibly supercritical (it is in the direction of steepest ascent depicted in Fig. 8) whereas the calculation is for subcritical topography. Clearly, the problem requires further investigation, but it does appear that the more sophisticated and much more technically complicated approach of applying the bottom boundary condition at $z = h(x, y)$ rather than $z = 0$ does not necessarily provide a better description of the interior response.

REFERENCES

Baines, P. B., 1973: The generation of internal tides by flat-bump topography. *Deep-Sea Res.,* **20,** 179–205.

Bell, T. H., 1975: Lee waves in stratified flows with simple harmonic time dependence. *J. Fluid Mech.,* **67,** 705–722.

Bender, C. M., and S. A. Orszag, 1978: *Advanced Mathematical Methods for Scientists and Engineers.* McGraw-Hill, 593 pp.

Cairns, J. L., and G. O. Williams, 1976: Internal wave observations from a midwater float, 2. *J. Geophys. Res.,* **81,** 1943–1950.

Duda, T. F., and C. S. Cox, 1989: Vertical wavenumber spectra of velocity and shear at small internal wave scales. *J. Geophys. Res.,* **94,** 939–950.

Egbert, G. D., A. F. Bennett, and M. G. G. Foreman, 1994: TOPEX/POSEIDON tides estimated using a global inverse model. *J. Geophys. Res.,* **99,** 24 821–24 852.

Gargett, A. E., P. J. Hendricks, T. B. Sanford, T. R. Osborn, and A. J. Williams III, 1981: A composite spectrum of vertical shear in the ocean. *J. Phys. Oceanogr.,* **11,** 1258–1271.

Garrett, C. J. R., and W. H. Munk, 1975: Space–time scales of internal waves. A progress report. *J. Geophys. Res.,* **80,** 291–297.

Goff, J. A., 1991: A global and regional stochastic analysis of near-ridge abyssal hill morphology. *J. Geophys. Res.,* **96,** 21 713–21 737.

——, 1992: Quantitative characterization of abyssal hill morphology along flow lines in the Atlantic Ocean. *J. Geophys. Res.,* **97,** 9183–9202.

——, and T. H. Jordan, 1988: Stochastic modeling of seafloor morphology: Inversion of Sea Beam data for second-order statistics. *J. Geophys. Res.,* **93,** 13 589–13 608.

Gregg, M. C., 1987: Diapycnal mixing in the thermocline: A review. *J. Geophys. Res.,* **92,** 5249–5286.

——, 1989: Scaling turbulent dissipation in the thermocline. *J. Geophys. Res.,* **94,** 9686–9698.

Hogg, N. G., P. Biscaye, W. Gardner, and W. J. Schmitz, 1982: On the transport and modification of Antarctic Bottom Water in the Vema Channel. *J. Mar. Res.,* **40,** 231–263.

Huang, R. X., and R. L. Chou, 1994: Parameter sensitivity study of the saline circulation. *Climate Dyn.,* **9,** 391–409.

Ledwell, J. R., A. J. Watson, and C. S. Law, 1993: Evidence for slow mixing across the pycnocline from an open-ocean tracer release experiment. *Nature,* **364,** 701–703.

——, E. T. Montgomery, K. L. Polzin, L. C. St. Laurent, R. W. Schmitt, and J. M. Toole, 2000: Evidence for enhanced mixing over rough topography in the abyssal ocean. *Nature,* **403,** 179–182.

McComas, C. H., and F. P. Bretherton, 1977: Resonant interaction of oceanic internal waves. *J. Geophys. Res.,* **82,** 1397–1412.

McDougall, T., 1991: Parameterizing mixing in inverse models. *Dynamics of Ocean Internal Gravity Waves: Proc. 'Aha Huliko'a Hawaiian Winter Workshop,* Honolulu, HI, University of Hawaii at Manoa, 355–386.

Müller, P., and N. Xu, 1992: Scattering of oceanic internal gravity waves off random bottom topography. *J. Phys. Oceanogr.,* **22,** 474–488.

Munk, W., 1966: Abyssal recipes. *Deep-Sea Res.,* **13,** 707–730.

Polzin, K. L., 1996: Statistics of the Richardson number: Mixing models and finestructure. *J. Phys. Oceanogr.,* **26,** 1409–1425.

——, 2004: A heuristic description of internal wave dynamics. *J. Phys. Oceanogr.,* **34,** 214–230.

——, J. M. Toole, and R. W. Schmitt, 1995: Finescale parameterizations of turbulent dissipation. *J. Phys. Oceanogr.,* **25,** 306–328.

——, ——, J. R. Ledwell, and R. W. Schmitt, 1997: Spatial variability of turbulent mixing in the abyssal ocean. *Science,* **276,** 93–96.

——, E. Kunze, J. M. Toole, and R. W. Schmitt, 2003: The partition of finescale energy into internal waves and subinertial motions. *J. Phys. Oceanogr.,* **33,** 234–248.

Rubenstein, D., 1988: Scattering of internal waves by rough bathymetry. *J. Phys. Oceanogr.,* **18,** 5–18.

Smith, W. H. F., and D. T. Sandwell, 1997: Global seafloor topography from satellite altimetry and ship depth soundings. *Science,* **277,** 1956–1962.

St. Laurent, L. C., and C. Garrett, 2002: The role of internal tides in mixing the deep ocean. *J. Phys. Oceanogr.,* **32,** 2882–2899.

——, J. M. Toole, and R. W. Schmitt, 2001: Buoyancy forcing by turbulence above rough topography in the abyssal Brazil Basin. *J. Phys. Oceanogr.,* **31,** 3476–3495.

Stommel, H., and A. B. Arons, 1960: On the abyssal circulation of the world ocean—I. Stationary planetary flow patterns on a sphere. *Deep-Sea Res.,* **6,** 140–154.

Wyrtki, K., 1961: The thermohaline circulation in relation to the general circulation in the oceans. *Deep-Sea Res.,* **7,** 39–64.